

RESEARCH ARTICLE

10.1002/2016JA023235

Key Points:

- Present methodologies for developing empirical models of ionospheric convection ignore polar cap expansion and contraction
- We propose normalizing measurements by the open-closed magnetic field line boundary location when developing models
- We demonstrate the impact of this methodology on climatological models of ionospheric vorticity

Correspondence to:

G. Chisham,
gchi@bas.ac.uk

Citation:

Chisham, G. (2017), A new methodology for the development of high-latitude ionospheric climatologies and empirical models, *J. Geophys. Res. Space Physics*, 122, 932–947, doi:10.1002/2016JA023235.

Received 26 JUL 2016

Accepted 19 DEC 2016

Accepted article online 22 DEC 2016

Published online 13 JAN 2017

A new methodology for the development of high-latitude ionospheric climatologies and empirical models

G. Chisham¹ 
¹ British Antarctic Survey, Cambridge, UK

Abstract Many empirical models and climatologies of high-latitude ionospheric processes, such as convection, have been developed over the last 40 years. One common feature in the development of these models is that measurements from different times are combined and averaged on fixed coordinate grids. This methodology ignores the reality that high-latitude ionospheric features are organized relative to the location of the ionospheric footprint of the boundary between open and closed geomagnetic field lines (OCB). This boundary is in continual motion, and the polar cap that it encloses is continually expanding and contracting in response to changes in the rates of magnetic reconnection at the Earth's magnetopause and in the magnetotail. As a consequence, models that are developed by combining and averaging data in fixed coordinate grids heavily smooth the variations that occur near the boundary location. Here we propose that the development of future models should consider the location of the OCB in order to more accurately model the variations in this region. We present a methodology which involves identifying the OCB from spacecraft auroral images and then organizing measurements in a grid where the bins are placed relative to the OCB location. We demonstrate the plausibility of this methodology using ionospheric vorticity measurements made by the Super Dual Auroral Radar Network radars and OCB measurements from the IMAGE spacecraft FUV auroral imagers. This demonstration shows that this new methodology results in sharpening and clarifying features of climatological maps near the OCB location. We discuss the potential impact of this methodology on space weather applications.

1. Introduction

Empirical models of the spatial variation of high-latitude ionospheric electrodynamic processes and characteristics, such as convection, magnetic field-aligned current, and vorticity, are useful tools which can advance the understanding of, and help the modeling and prediction of, space weather processes in the magnetosphere-ionosphere-thermosphere system. Often, these models are climatological averages of measured quantities, portraying the spatial variation of these averages across the polar ionosphere during intervals with similar background conditions (e.g., time of year) and driving conditions (e.g., interplanetary magnetic field (IMF) strength and direction). These climatologies can be especially useful when subdivided for a wide range of conditions, providing good large-scale representations of ionospheric electrodynamic processes.

Climatological averages cannot be viewed as providing instantaneous pictures of ionospheric electrodynamic processes for a particular time, due to the high variability of the ionospheric response to driving factors and background conditions. The climatologies can, however, form the basis of more sophisticated methods for representing ionospheric variations involving data assimilation, such as Assimilative Mapping of Ionospheric Electrodynamics (AMIE) [e.g., Richmond, 1992] or Super Dual Auroral Radar Network (SuperDARN) global convection mapping (known colloquially as "Map Potential") [Ruohoniemi and Baker, 1998]. Hence, accurate and high-resolution climatological models are highly desirable.

Probably, the most often modeled ionospheric electrodynamic process is convection; responsible for the large-scale motion of plasma within the Earth's magnetosphere. Representations of the ionospheric convection electric field, generally in the form of electrostatic potential maps, have been produced for decades [e.g., Heppner, 1972, 1977]. The average spatial variation of the electrostatic potential in the high-latitude ionosphere has been determined from databases of electric field measurements from thermal ion drift data measured by low Earth-orbiting spacecraft crossing the polar regions, such as the Dynamics Explorer 2 (DE 2) and Defense Meteorological Satellite Program (DMSP) spacecraft [e.g., Heppner and Maynard, 1987; Rich and Maynard, 1989; Rich and Hairston, 1994; Weimer, 1995, 2001a, 2005; Papitashvili and Rich, 2002], and also from

direct electric field measurements from the Cluster spacecraft in higher Earth orbit [e.g., *Haaland et al.*, 2007]. Databases of ion drift data from ground-based radars such as incoherent scatter radars (ISR) and the global network of SuperDARN HF coherent scatter radars have also been successfully used to produce climatological patterns of convection in the form of electrostatic potential maps [e.g., *Holt et al.*, 1987; *Foster et al.*, 1989; *Ruohoniemi and Greenwald*, 1996, 2005; *Peymirat and Fontaine*, 1997; *Zhang et al.*, 2007; *Pettigrew et al.*, 2010; *Cousins and Shepherd*, 2010]. Some of these models are purely statistical climatological representations, but more recent studies have involved the fitting of basis functions such as spherical harmonics to data covering the whole polar ionosphere, to provide a more practically usable product [e.g., *Weimer*, 1995; *Papitashvili and Rich*, 2002; *Zhang et al.*, 2007]. However, such fitting does often have the downside of smoothing smaller-scale features in the climatological patterns.

Although much of the focus of ionospheric climatologies has been the convection electric field, other aspects of ionospheric electrodynamics have also been addressed. These include the magnetic field-aligned currents (FACs) that transfer energy and momentum between the magnetosphere and ionosphere [e.g., *Foster et al.*, 1989; *Weimer*, 2001b, 2005; *Anderson et al.*, 2008] and the related quantity of field-aligned vorticity of the ionospheric plasma [*Chisham et al.*, 2009]. Ionospheric vorticity provides a measure of the dynamical coupling of the magnetosphere to the ionosphere via FACs. Indeed, ionospheric vorticity measurements have often been used as proxy measurements for FACs [*Sofko et al.*, 1995; *McWilliams et al.*, 2001]. In addition, *Weimer* [2005] combined climatological models of electric potential, magnetic potential, and FAC in the ionosphere, resulting in the determination of models of Poynting flux and Joule heating.

It has long been known (since, e.g., *Heppner* [1972]) that the morphology of ionospheric electrodynamics, especially in the dayside ionosphere, is heavily dependent on the state of the IMF driver, particularly the direction of the field as projected into the plane perpendicular to the Earth-Sun line (the IMF clock angle direction). This clock angle direction controls the preferred sites where magnetic reconnection occurs on the Earth's dayside magnetopause [*Dungey*, 1961; *Russell*, 1972; *Cowley*, 1981]. Magnetic reconnection is responsible for changing the topology of geomagnetic field lines between the higher-latitude "open" field line region, where magnetic field lines have one end attached to the Earth and one that extends into interplanetary space (as in the polar cap region), and the lower latitude "closed" field line region, where magnetic field lines have both ends attached to the Earth in different hemispheres. The IMF also influences the motion of newly reconnected magnetic field lines advecting through the magnetosphere to the magnetotail. This controls the motion of the footprints of the magnetic field lines across the ionospheric polar cap region and hence the pattern of the ionospheric convection, FACs, and vorticity, in this region. Hence, it has always been deemed important to develop separate ionospheric climatologies or models for a range of different IMF conditions [e.g., *Heppner*, 1977].

Another factor that is often considered in the development of climatologies and models is that of the tilt of the Earth's magnetic field with respect to the plane perpendicular to the Earth-Sun line (the dipole tilt) which varies with both time of day and time of year. Variation in the dipole tilt affects the location of magnetic reconnection on the dayside magnetopause [e.g., *Russell et al.*, 2003], and hence the consequent plasma flow and current systems within the magnetosphere and ionosphere. It also varies the spatial distribution of ionospheric conductance in the polar regions in the two hemispheres due to the variation in photoionization in the polar ionospheres [e.g., *Ridley*, 2007]. This is particularly important for climatologies of FACs which are heavily affected by variations in conductance.

Whereas the two factors discussed above are regularly considered in the development of ionospheric climatologies and models, there are other factors that are rarely considered, yet can have a significant effect on the spatial picture of ionospheric electrodynamics. One such factor is the effect of the expanding/contracting nature of the polar cap, which has significant control over the morphology of ionospheric plasma flow. The size of the polar cap varies greatly due to the continual, and unequal, changes in the rates of magnetic reconnection on the dayside and nightside of the magnetosphere [e.g., *Chisham et al.*, 2008a]. In this paper we concentrate solely on the effects of this one factor, although there is, in fact, significant overlap with other factors as addressed in section 5 of this paper.

The polar cap is enclosed by the ionospheric footprint of the open-closed magnetic field line boundary (OCB). This is the magnetospheric boundary between the regions of open and closed magnetic field line topologies. Hence, it is at this boundary that magnetic reconnection occurs. Changes in the size of the polar cap are linked to variations in the rate of magnetic reconnection, with the addition of open flux resulting from reconnection

between geomagnetic field lines and the IMF on the dayside of the Earth and the closure of open flux resulting predominantly from reconnection within the magnetotail on the nightside of the Earth [Siscoe and Huang, 1985]. Due to the continually varying, and unequal, rates of dayside and nightside reconnection, the OCB is in constant motion, expanding to lower latitudes during intervals when the IMF is predominantly southward and dayside reconnection is enhanced, and contracting when it is predominantly northward which allows nightside reconnection to remove open magnetic flux from the polar cap at a faster rate than it is added on the dayside.

The morphology of large-scale ionospheric electrodynamic variations such as convection and FAC are ordered relative to the OCB location [e.g., Cowley and Lockwood, 1992]; the direction of convection can change relatively sharply at this boundary, associated with increased FACs and vorticity. However, in the development of most climatologies, measurements of the chosen parameter are generally binned for averaging according to their position in either a fixed geographic or geomagnetic coordinate system and not their position relative to the OCB location. Not considering the changing size of the polar cap, and hence the changing location of this boundary, distorts the shape of the resulting climatological patterns; e.g., sharp variations in the patterns near the OCB will not be fully captured. Hence, the resulting spatial patterns are smoother and more averaged when compared to individual measurements made by both ground-based radars and low-altitude spacecraft. As an exception to this typical approach, Rich and Hairston [1994] used a coordinate system which expanded and contracted to compensate for motion of the auroral oval with changing geomagnetic activity level. They adjusted the magnetic coordinates of satellite tracks so that the measured oval matched the location of that observed for $K_p = 3+$. They concluded that this methodology reduces the spreading of the average pattern which results from fluctuations in the size of the auroral oval (which are related to fluctuations in the size of the polar cap). A similar approach was used by Sotirelis and Newell [2000] to organize the signatures of precipitating electrons in the polar ionosphere. They concluded that this approach resulted in models that more closely resembled instantaneous observations.

We propose a similar methodology for the future development of climatologies and models that considers the location and motion of the OCB. In this methodology, the data used to develop the empirical model or climatology are mapped into a coordinate frame that is relative to the OCB location, rather than onto a fixed geographic or geomagnetic grid. The aim is to produce climatologies and models that reproduce more closely the variations in parameters that are typically seen in the vicinity of the OCB.

To provide a demonstration of the effect of the proposed methodology, we address the comparatively easy example of climatological maps of ionospheric vorticity. Chisham *et al.* [2009] developed a technique to measure the magnetic field-aligned vorticity of plasma flow in the *F* region ionosphere using line-of-sight velocity measurements made by SuperDARN. They produced climatological maps of average ionospheric vorticity across the Northern Hemisphere ionosphere using 6 years (2000–2005 inclusive) of SuperDARN data and showed that the spatial variation of average vorticity is well organized according to the well-established large-scale FAC structure in the polar ionosphere. However, they did not consider the changing location of the OCB, and hence did not account for the movement of the vorticity pattern in response to changes in the size of the polar cap, consequently smoothing the resulting climatological vorticity maps.

For this demonstration we require simultaneous measurements of the OCB location and ionospheric vorticity. The location of the OCB is most accurately measured using in situ measurements of particle precipitation boundaries made by spacecraft in low-altitude orbits, such as the DMSP spacecraft [e.g., Newell *et al.*, 1991, 1996]. However, these spacecraft typically provide only infrequent, single-point measurements of the OCB. Considering that the OCB can move up to $\sim 0.2^\circ/\text{s}$ [e.g., Sotirelis *et al.*, 1998], building up a complete picture of the OCB across the whole polar ionosphere on a timescale that would capture most of the boundary motion is difficult. Arguably, the best instruments that can measure the complete OCB location (in a single hemisphere) are satellite-based auroral imagers, which can image the whole auroral oval at a time resolution of the order of minutes, for hours at a time [see, e.g., Boakes *et al.*, 2008; Longden *et al.*, 2010]. The poleward edge of the UV auroral oval often provides a very good proxy for the OCB location, although this can depend on the sensitivity of the imager and the auroral brightness. Here we use OCB measurements determined from far ultraviolet (FUV) imager data of the Northern Hemisphere auroral region from the Imager for Magnetopause-to-Aurora Global Exploration (IMAGE) spacecraft [Mende *et al.*, 2000a]. To estimate the OCB location, we extend the methodology of Longden *et al.* [2010], who developed a reliable, automated method to estimate the location of the poleward auroral luminosity boundary (PALB) from the FUV images.

This paper is structured as follows: In section 2 we discuss the instrumentation used to provide the data for this demonstration; in section 3 we discuss the methodologies for determining the OCB and ionospheric vorticity, and for binning and scaling the vorticity data; in section 4 we present the results of the demonstration; and in section 5 we discuss the implications of this demonstration for the development of future ionospheric climatological and empirical models.

2. Instrumentation

2.1. IMAGE FUV

Auroral images from the IMAGE FUV instrument are available for the epoch May 2000 until December 2005. In this study, we use data from between May 2000 and August 2002, during which time the satellite apogee was over the northern polar region, providing large intervals of time with complete images of the northern polar aurora. During this time, the spacecraft was stationed in an elliptical orbit at 90° inclination, with an altitude of $7 R_E$ at apogee (above the northern polar region) and 1000 km at perigee (above the southern polar region), and with an orbital period of ~ 13.5 h.

The results presented in this paper have used data from the Spectrographic Imager SI13 [Mende *et al.*, 2000c], although data from the Spectrographic Imager SI12 [Mende *et al.*, 2000c] and the Wideband Imaging Camera (WIC) [Mende *et al.*, 2000b] were also used in comparative analyses, but are not shown. The SI13 detector measured oxygen emissions at 135.6 nm resulting from energetic electron precipitation. The SI12 detector measured Doppler-shifted Lyman- α emissions at 121.8 nm, that result as a consequence of proton precipitation. The WIC sensor was sensitive to emissions with wavelengths in the range 140 to 190 nm, and observed emissions from the N2 Lyman-Birge-Hopfield band, resulting from electron precipitation. The images from all the detectors were taken at a time resolution of approximately 2 min (determined by the spin period of the spacecraft). The SI detectors produced images with a 128×128 pixel resolution, whereas the WIC detector had a resolution of 256×256 pixels. The images have been converted into an Altitude-Adjusted Corrected GeoMagnetic (AACGM) coordinate frame for consistency with the ionospheric vorticity measurements.

2.2. SuperDARN

SuperDARN [Greenwald *et al.*, 1995; Chisham *et al.*, 2007] is a network of coherent scatter radars whose combined fields of view cover extensive regions of the Northern and Southern Hemisphere polar ionospheres. The radars transmit radio signals in the high-frequency (HF) band (between 8 and 20 MHz) on oblique propagation paths which are refracted toward the horizontal in the ionosphere due to the changing refractive index they encounter in the *E* and *F* region ionosphere. These signals can backscatter from decameter-scale ionospheric magnetic field-aligned density irregularities in the ionosphere and be received back at the radar. The radars are able to measure the Doppler line-of-sight velocity of the irregularities that move at the $E \times B$ drift velocity of the background plasma in the *F* region ionosphere [Villain *et al.*, 1985]. Velocity measurements across the complete SuperDARN field of view are typically made with a 1 or 2 min cadence.

Figure 1 shows the fields of view of the six Northern Hemisphere SuperDARN radars used in this study. Three pairs of radars with overlapping fields of view are used. The blue and green lines represent the central look directions of the 16 beams along which measurements are made for each radar. These beams are colored red in regions where the beams from different radars overlap (and hence where vorticity measurements can be made). The mapping of the fields of view used in this paper employs the empirical virtual height model of Chisham *et al.* [2008b] which has been shown to map far-range backscatter more accurately than other presently available virtual height models (as described in Yeoman *et al.* [2008]).

3. Methodology

3.1. OCB Location Estimation

We have developed a three-stage process for estimating the OCB location in the northern polar ionosphere. This comprises the following:

1. Identifying the PALB in latitudinal profiles of auroral intensity in different magnetic local time (MLT) sectors (as in Carbary *et al.* [2003], Boakes *et al.* [2008], and Longden *et al.* [2010]);
2. Applying latitudinal corrections at each MLT based on the average offset measured between multiple PALB measurements and more accurate proxies for the OCB (as discussed in Carbary *et al.* [2003], Boakes *et al.* [2008], and Longden *et al.* [2010]);

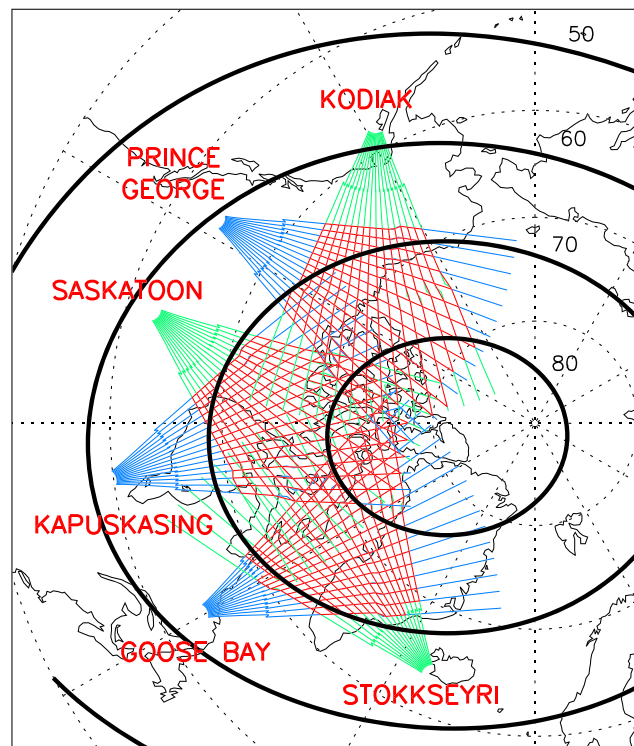


Figure 1. The fields of view of the six Northern Hemisphere SuperDARN radars used in this study (green and blue lines represent the beam directions). The red lines highlight the quadrilateral measurement cells that are formed by overlapping beams from adjacent radars and which form the closed loops for the vorticity determination. The bold black lines show AACGM latitude contours at 10° intervals.

3. Fitting a model circle to the corrected OCB estimates at all MLTs to provide an easily scalable boundary location estimate covering the whole polar ionosphere.

Figure 2 presents examples of this process, as detailed in the following sections. Throughout this process we use the coordinate system of AACGM latitude and MLT.

3.1.1. Identifying the PALB From Latitudinal Auroral Intensity Profiles

To identify the PALB in the latitudinal profiles of auroral intensity, we follow the methodology of Longden *et al.* [2010]. This method allows the estimation of the PALB without prior knowledge of the level of auroral activity or the presence of bifurcation of the auroral oval. Full detail of the method, with example applications and discussion of the treatment of dayglow, can be found in that paper. Here we provide only a brief explanation of the methodology:

1. Each auroral image is divided into 24 latitudinal intensity profiles in an AACGM latitude and MLT coordinate system, each profile covering a 1 h segment of MLT.
2. For each 1 h MLT segment, the intensity profile is constructed by finding the average auroral intensity in bins of 1° AACGM latitude in the range of 50° to 90° .
3. Two separate model functions are fitted to each latitudinal intensity profile: (i) A function with a single Gaussian component and a quadratic background—this provides a good model of the latitudinal auroral intensity variation when the auroral emission forms a single continuous oval. (ii) A function with two Gaussian components and a quadratic background—this provides a better model of the auroral intensity variation when the oval shows bifurcation (see Longden *et al.* [2010] for more detail, full justification, and example fits). These fits provide estimates of the amplitude, central location, and width of the peaks in the intensity profile.
4. Of the two fitted functions, the better model is chosen by determining the reduced chi-square goodness-of-fit statistic for both functions. This is performed separately for each latitudinal intensity profile at each MLT.
5. When the single Gaussian function provides the better fit, the location of the PALB is estimated as being offset poleward from the location of the center of the Gaussian peak by the full width at half maximum

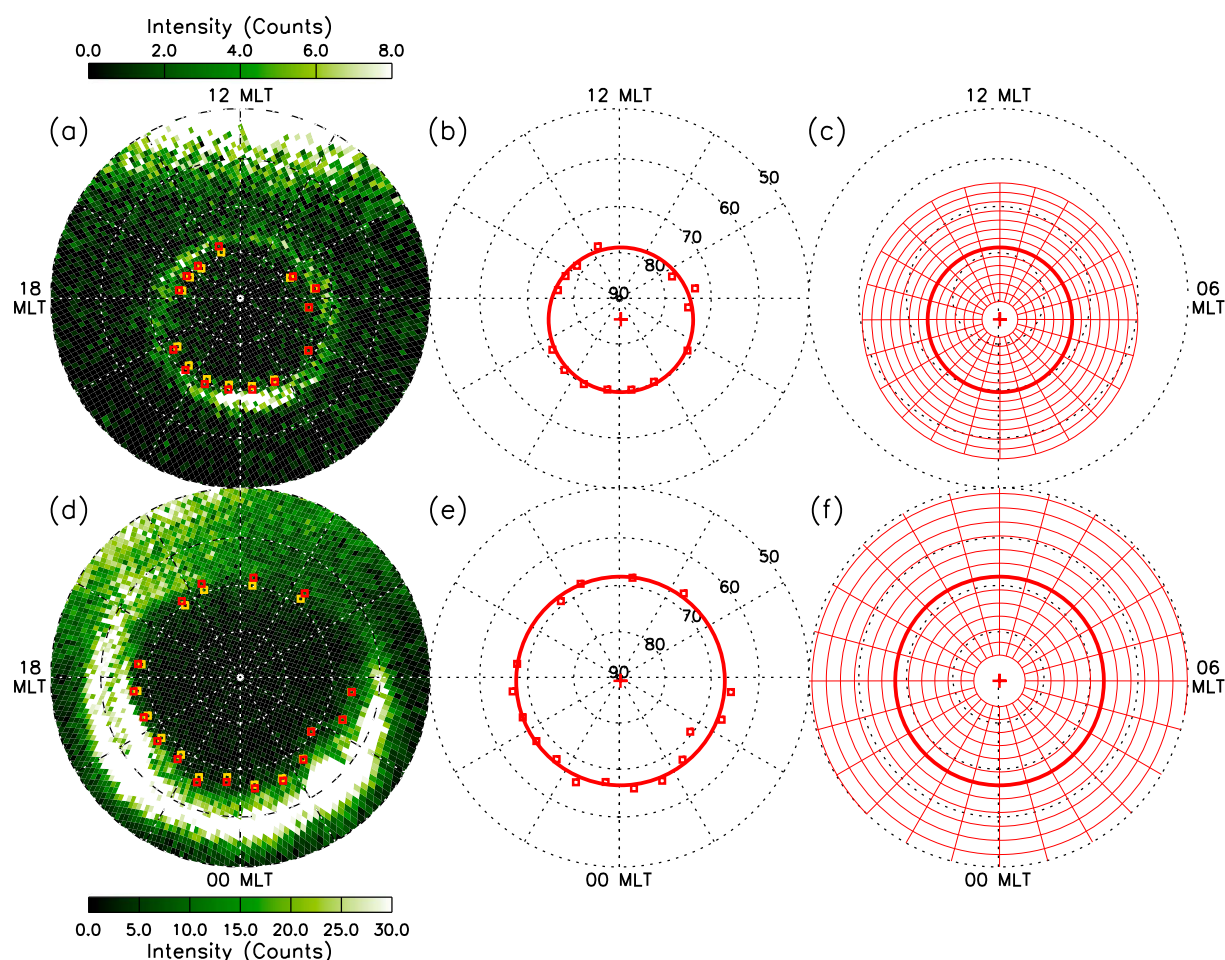


Figure 2. Two examples of the methodology used to determine the circular OCB boundary fits from SI13 auroral images and the OCB-normalized coordinate system from the OCB location. (a–c) Data from 02:38 UT on 6 December 2000, (d–f) data from 09:17 UT on 28 October 2001. Figures 2a and 2d present the SI13 auroral images for these times. The yellow square symbols represent poleward auroral luminosity boundary (PALB) estimates determined from the IMAGE FUV SI13 images at a 1 h MLT resolution, using the method of Longden *et al.* [2010]. The red square symbols represent the corrected locations of these PALB estimates using the corrections outlined in Longden *et al.* [2010]. Figures 2b and 2e present the OCB circle fits to the corrected PALB locations. The solid red line represents the best circular fit to these boundary estimates using the method of Umbach and Jones [2003]. The red cross represents the center of the fitted circle. Figures 2c and 2f present the binning structures in the OCB-normalized frame determined from the OCB circle fits. All panels are in AACGM coordinates.

(FWHM) of the peak (as in Carbary *et al.* [2003], Boakes *et al.* [2008], and Longden *et al.* [2010]). When the double Gaussian function provides the better fit, the location of the PALB is estimated as being offset poleward from the location of the peak of the most poleward of the two Gaussian components by the FWHM. (In the nightside MLT sectors, up to ~35% of PALB estimates are determined from double Gaussian fits to the latitudinal auroral intensity profiles, in preference to single Gaussian fits).

6. Finally, a number of criteria are applied during the fitting process to discard poorly estimated PALB locations arising from either poor fitting or incomplete data (see Longden *et al.* [2010] for full details and justifications for these criteria).

Figure 2 presents two examples of the results of this boundary estimation process, one for a small, weak auroral oval, and one for a large, intense auroral oval. Figure 2a presents an SI13 image of the Northern Hemisphere auroral oval from 02:38 UT on 6 December 2000, when the oval was small and characterized by low intensity. The yellow symbols in this figure (some of which are obscured by the red symbols, as discussed below) highlight the PALB locations determined for this interval using the methodology above. For comparison, Figure 2d also presents an SI13 image of the Northern Hemisphere auroral oval, but from 09:17 UT on 28 October 2001, when the oval was much larger and more intense, and characterized by bifurcations in some MLT sectors. Again, the yellow symbols highlight the PALB locations at this time. Note that there are some MLT sectors in both examples where it was not possible to determine a reliable PALB estimate and no boundary is shown.

3.1.2. Correcting PALB Estimates to Provide the Best Estimates of the OCB Location

Due to the complexities of how different precipitating particles of different species and energy relate to the OCB location, the PALBs derived from FUV auroral images do not always provide an exact match in latitudinal location with more accurate proxies for the OCB, such as the particle precipitation boundaries determined from measurements made by low-altitude spacecraft such as DMSP [Carbary *et al.*, 2003; Boakes *et al.*, 2008; Longden *et al.*, 2010]. This results in a series of systematic offsets between the PALB and the true OCB that vary with MLT. In order to make the best possible estimates of the OCB from the PALB locations, we employ a series of corrections to minimize these systematic offsets. Longden *et al.* [2010] derived corrections to the estimated PALB latitudes for each of the different FUV imagers and for each 1 h MLT sector (see their Figure 9 and Table 4). These corrections were determined by minimizing the unknown measurement errors in large-scale statistical comparisons of PALBs and DMSP particle precipitation boundaries (see Boakes *et al.* [2008] and Longden *et al.* [2010] for full details). This is the most effective way of adjusting for the systematic offsets, although random errors in the estimated boundary locations are still likely to remain.

In Figures 2a and 2d the corrected boundary locations are shown by the red symbols. In the early morning sector the corrections are very small and so the boundaries move very little in comparison to the uncorrected PALBs (yellow symbols). In other MLT sectors the correction offset can be clearly seen, moving the boundary estimates equatorward by $\sim 1^\circ - 2^\circ$ AACGM latitude. As a consequence of this offset removal, the corrected data set provides boundary estimates that are very consistent between the three FUV imagers and more consistent with estimates of the OCB from other instrumentation [Longden *et al.*, 2010]. This justifies our decision to use the results from a single imager (SI13) in this study.

3.1.3. Fitting a Circle to the OCB Estimates

Successfully employing our proposed methodology requires an easily scalable representation of the OCB location at all MLTs. However, as discussed above, the FUV PALB measurements do not always cover all MLT sectors, with gaps a regular occurrence, especially in the dayside ionosphere where dayglow can be an issue. Hence, we choose to fit a simple and practical model function, a circle, to the available corrected PALB measurements (our best estimates of the OCB location) in order to fill these data gaps, providing our best estimate of a model boundary that covers all MLTs. Off-center circles in geomagnetic coordinate systems have been used for some time to model the location of the PALB [e.g., Holzworth and Meng, 1975; Meng *et al.*, 1977].

To fit a circle to the corrected PALB data from a particular time, we use the modified least squares method of Umbach and Jones [2003]. Each fitted circle is defined by three parameters; two representing the coordinates of the center of the circle (the latitudinal offset from the pole r_c and the MLT of the circle center location ϕ_c) and the distance from the center of the circle to the circumference (R_b). (Both r_c and R_b are expressed as a colatitude, in degrees). Figures 2b and 2e present examples of the circle fitting process for the two SI13 images discussed above (shown in Figures 2a and 2d). The red symbols once again represent the corrected PALB locations estimated from the 1 h MLT sector latitudinal profiles. The solid red circle represents the best fit circle to the available boundary estimates, which provides a good fit to the data for the intervals shown. The red plus symbol shows the location of the center of the fitted circle.

A series of criteria have been developed in order to discard fits when the fitting is poor or unrealistic. These criteria have been developed by examining the probability distributions of the fitted parameters (not shown) for the whole 2 year data set. The criteria are as follows:

1. Discard fits at times when there are less than seven individual OCB estimates being fitted to (i.e., measurements in less than seven 1 h MLT sectors): The probability distributions of the fitted parameters, although approximately constant for intervals when there are seven or more OCB estimates available, are characterized by an increasing variance as the number of OCB estimates reduces below seven, suggesting a significant increase in random errors introduced by fitting to limited data.
2. Discard fits where $R_b > 23^\circ$ or $R_b < 10^\circ$: The distributions of R_b for fits involving large numbers of individual OCB estimates (e.g., greater than 20—for which the fits are most reliable) remain strictly within this bound ($10^\circ - 23^\circ$), suggesting that measurements of R_b outside this range, for instances when we have a smaller number of OCB estimates, are a result of increased random error.
3. Discard fits where $r_c > 8^\circ$: The distributions of r_c for fits involving large numbers of individual OCB estimates remain strictly below 8° , and hence, the same argument is made as in point (2) above.

It is possible that application of these criteria may exclude instances when the OCB is not well represented by a circle. It may be that future developments of this methodology could allow greater flexibility in the model for the OCB shape (e.g., an elliptical representation).

3.2. Vorticity Determination Method

We calculate the ionospheric magnetic field-aligned plasma flow vorticity from line-of-sight velocity measurements made by the SuperDARN HF radars, using the methodology developed by *Chisham et al.* [2009]. This method employs Stokes' theorem

$$\oint_C \mathbf{v} \cdot d\mathbf{l} = \int_S \omega \cdot d\mathbf{S} \quad (1)$$

to determine the vorticity, ω , at different locations across the overlapping SuperDARN fields of view by approximating $\mathbf{v} \cdot d\mathbf{l}$ around diamonds defined by the geometry of the SuperDARN radar beams (see Figure 1), which represent closed loops, C , enclosing surfaces, S [see *Chisham et al.*, 2009, Figure 2]. The $\mathbf{v} \cdot d\mathbf{l}$ is determined from the discrete velocity measurements and line segments relating to individual line-of-sight velocity measurements (see *Chisham et al.* [2009] for full detail). This methodology has similarities to that of *Sofko et al.* [1995], which also determines vorticity using SuperDARN data, but this methodology contains fewer assumptions and limitations.

The study of *Chisham et al.* [2009] used vorticity values from 1 and 2 min common mode SuperDARN radar scans during the 6 year epoch 2000–2005. In this study we use the subset of this data set which overlaps with the Northern Hemisphere IMAGE FUV data set (May 2000 to August 2002).

3.3. Binning the Vorticity Data

The climatological average vorticity maps presented in this paper involve spatially mapping the vorticity data in different ways in order to demonstrate the impact of binning the data relative to the OCB location.

First, the vorticity data are binned in the fixed AACGM latitude and MLT coordinate frame, as in *Chisham et al.* [2009]. Here the vorticity data are sorted into spatial bins of size 1 h of MLT by 2° of AACGM latitude, based on where the centers of the relevant vorticity measurement cells are located. (The latitude bins are larger than the 1° bins of *Chisham et al.* [2009] because of the reduced data set used in this study). The mean vorticity value in every spatial bin is then determined, providing the climatological average pattern.

Second, the vorticity data are binned in the OCB-normalized frame. Determining the layout of the bins in this frame requires choosing the number of “latitude” (in quotes as the circle center is typically shifted away from the AACGM pole) bins within which the data are organized within the fitted OCB circle (termed N_l). These bins will be equally spaced in latitude in the OCB-normalized frame between the fitted OCB circle and the “pole” in the OCB-normalized frame (which is the center of the circle (r_c, ϕ_c) in the AACGM coordinate system). The size and position of these bins will vary from one data interval to the next as the size and position of the fitted OCB circle varies. The choice of the number of “latitude” bins depends heavily on the amount of data available, as there need to be enough measurements in each bin to produce a reliable average vorticity value in each bin. Through trial and error we have selected $N_l = 8$ for the analysis in this paper, although this can be increased in future analyses to provide better spatial resolution if more data are available. The “latitude” bins outside (equatorward of) the fitted OCB circle are chosen so that they have the same “latitudinal” extent as those inside the circle. As when binning in the geomagnetic coordinate system we divide the data into twenty-four 1 h MLT sectors.

Figures 2c and 2f illustrate this variable binning grid for our two example intervals. Here we only highlight six of the eight latitude bins within the OCB as those at higher latitude become increasingly small, and consequently contain very little data. The different extents of the bins in the two examples, which result from the large differences in the polar cap size, are very clear from comparing the two figures. Although the size and location of individual bins is different in the two examples, the relationship of each bin to the OCB, when normalized to the OCB frame, is the same.

Third, the vorticity data are binned in the same OCB-normalized frame, but also in four subgroups relating to the prevailing IMF direction, to see how the established variations with the IMF are reproduced. Each subgroup relates to a 90° IMF clock angle bin in the GSM Y-Z plane. To determine the IMF clock angle at any time, we use Weimer-mapped IMF data from the ACE spacecraft [*Weimer et al.*, 2002] which provides accurate mapping of the data from the ACE spacecraft to the magnetosphere. We restrict our analysis to relatively stable IMF

intervals; we choose stable intervals by subdividing the mapped IMF data into half-hour intervals and only including vorticity data from those intervals for which more than 70% of the IMF data were in a single clock angle bin.

3.4. Scaling the Vorticity Values

When binning ionospheric convection measurements in a fixed geomagnetic coordinate grid (whether they be measurements of vorticity, as in this paper, or of velocity or electric potential), the spatial pattern that results from the averaging of data on this fixed grid has a fixed potential drop across the polar cap associated with it. This is clearly shown in many climatologies of ionospheric convection [e.g., *Weimer, 2005; Ruohoniemi and Greenwald, 2005; Pettigrew et al., 2010*], where the cross-polar cap potential values are explicitly given for each map. The magnitude of this potential drop only varies between the different patterns that are determined for different conditions (e.g., for different IMF clock angle directions). Generally implicit in this assumption is that the variability that exists in the cross-polar cap potential drop, due to the variability of nightside reconnection, is averaged out.

When binning ionospheric convection measurements on a coordinate grid which is of variable size and not fixed in space (e.g., in our OCB-normalized frame), we choose to make the same assumption in order to produce a single averaged pattern, i.e., that the potential drop across the polar cap in the climatological pattern is fixed irrespective of the size of the polar cap. As the size of the polar cap, and hence, the size of our coordinate system, varies from measurement to measurement, the vorticity values need to be scaled before averaging to compensate for this variation. We choose to scale our measurements to a fixed circular polar cap of a “typical” size with radius R_n —the value of R_n can be anything, but if set to the size of the average OCB distance from the circle center, the vorticity values in the resulting climatological maps will be of similar magnitude to those in fixed geomagnetic coordinate systems.

If we initially consider the effects on electric field measurements, those made in a geomagnetic coordinate grid (E_G) must be scaled to a value (E_*) in the OCB-normalized grid, using

$$E_G R_b = E_* R_n \quad (2)$$

where R_b is the radius of the fitted OCB circle (as discussed above). Hence, when the measured polar cap is larger than our typical polar cap ($R_b > R_n$), we need to increase the electric field value (when converting from E_G to E_*) so that we achieve the same potential drop over a smaller region. Similarly, when the measured polar cap is smaller than our typical polar cap ($R_b < R_n$), we need to decrease the electric field value to achieve the same potential drop over a larger region. Hence, following the above equation, the scaling for electric field measurements is therefore

$$E_* = \frac{E_G R_b}{R_n} \quad (3)$$

The same arguments can also be applied if we consider the effects on convection velocity and vorticity. Assuming that the geomagnetic field varies only marginally over the high-latitude region, the scaling for the electric field measurements is replicated for convection velocity measurements, i.e.,

$$v_* = \frac{v_G R_b}{R_n} \quad (4)$$

As vorticity $\omega = \nabla \times v$, then the scaling for the vorticity measurements is

$$\omega_* = \frac{\omega_G R_b^2}{R_n^2} \quad (5)$$

Hence, all the measured vorticity values must be scaled in this way before the measurements in each spatial bin are averaged.

The final averaged model patterns that result from this analysis (which will be calculated for the typical polar cap radius R_n) can be scaled to the polar cap size required (using the reverse of this scaling method) when the model is used in any analyses or applications.

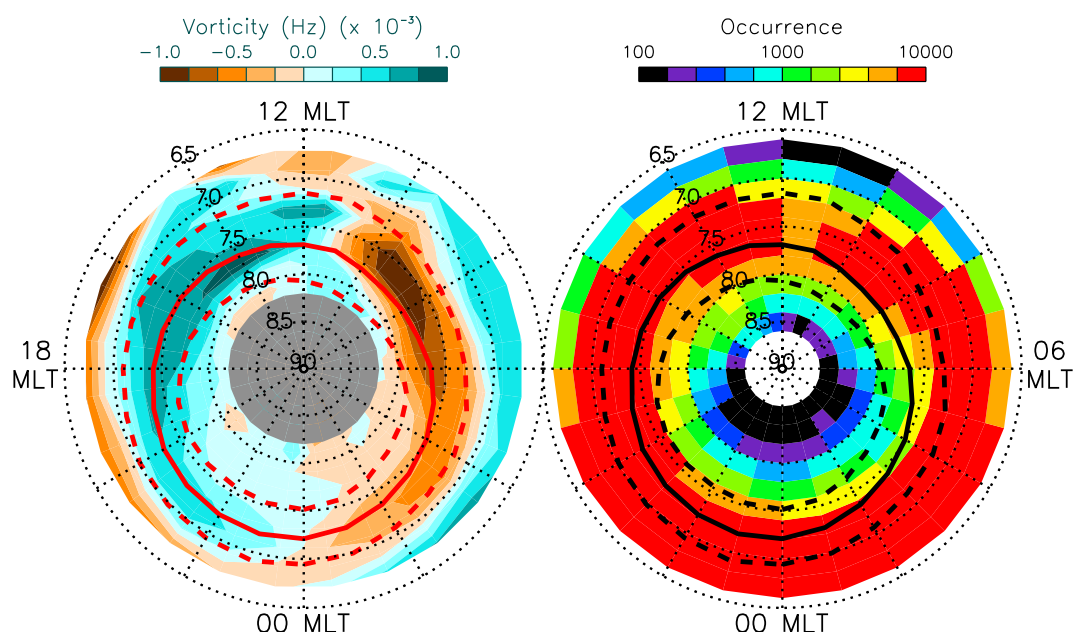


Figure 3. (left) The spatial distribution of average vorticity measured by the six SuperDARN radars, for the intervals during which a circular OCB fit could be made to the IMAGE FUV S113 boundaries, in AACGM coordinates. The contours are determined from data binned in bins of 2° AACGM latitude by 1 h of MLT. (right) The number of vorticity measurements in each bin used in the determination of the average vorticity. The solid lines represent the median OCB location for all the intervals used. The dashed lines represent the 10th and 90th percentiles of the OCB location.

4. Results

4.1. Fixed Geomagnetic Coordinate System

Figure 3 presents a contour plot of the spatial variation of average vorticity across the Northern Hemisphere polar ionosphere when the vorticity data are binned in the fixed AACGM latitude and MLT coordinate system (Figure 3, left) (this map includes data for all IMF orientations). This figure effectively presents the average vorticity variation in the same way as *Chisham et al.* [2009] but using a reduced data set (only those intervals for which an OCB location can be determined from the FUV auroral images), which has necessitated a reduction in the latitudinal resolution from 1° to 2° . In this figure the orange shading relates to a negative vorticity (anticlockwise rotation looking down on the Northern Hemisphere ionosphere) and the blue shading relates to a positive vorticity (clockwise rotation). The solid red line presents the MLT variation of the median OCB location for the intervals used in this analysis. The dashed red lines present the 10% and 90% percentiles of the OCB location in all MLT sectors. Figure 3 also shows the number of vorticity measurements contributing to the average value in each MLT-latitude bin (Figure 3, right). This figure shows that there are ~ 1000 or more measurements in most bins, especially those close to, and equatorward of, the median OCB location; these large samples provide confidence in the stability of the average vorticity values in each bin.

As expected, the average vorticity map shows the same general spatial features as that in *Chisham et al.* [2009] which used 6 years of vorticity data (2000–2005). This spatial variation is similar to the average picture of the distribution of large-scale field-aligned currents, particularly the locations of the region 1 (R1) and region 2 (R2) current systems, as described fully in *Chisham et al.* [2009]. At the lower latitude edge of the field of view ($< \sim 70^\circ$) the morning sector is characterized by positive vorticity, whereas the afternoon sector is characterized by negative vorticity. At higher latitudes (between $\sim 70^\circ$ and $\sim 80^\circ$) the direction of the vorticity in both the morning and afternoon switches, mimicking the transition from R2 to R1 FACs. One difference to the results of *Chisham et al.* [2009] is that there is reduced evidence of the existence of vorticity regions corresponding to the NBZ current system at high latitudes ($\sim 80^\circ$) in the dayside ionosphere. This is most likely a result of the reduced data set used in this study.

4.2. OCB-Normalized Coordinate System

Figure 4 presents a contour plot of the spatial variation of average vorticity across the Northern Hemisphere ionosphere when the vorticity data is binned in the OCB-normalized coordinate system (Figure 4, left).

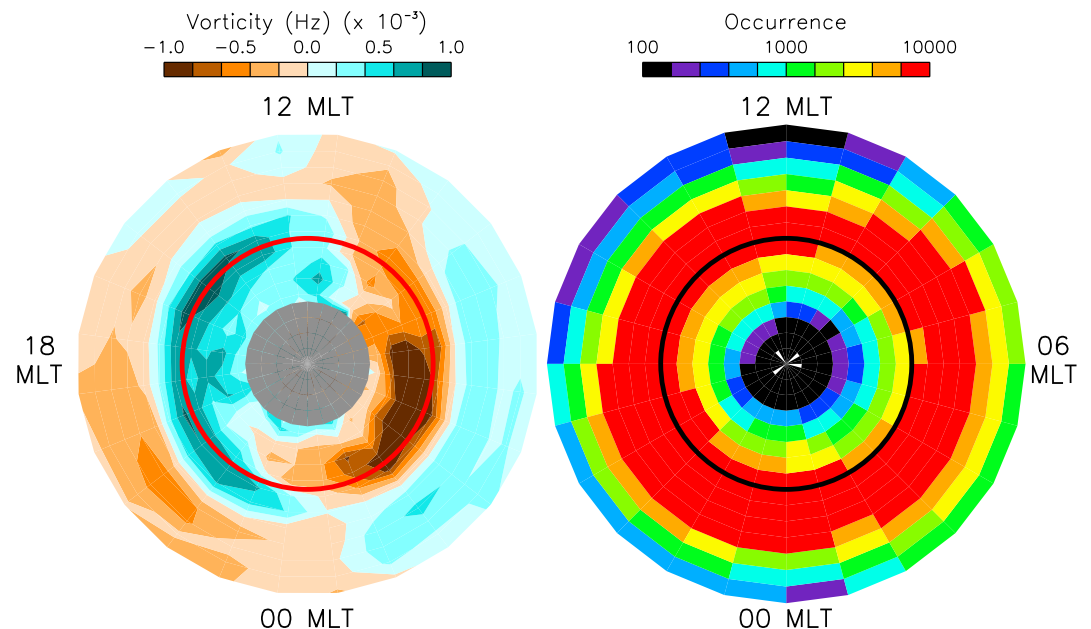


Figure 4. (left) The spatial distribution of average vorticity measured by the six SuperDARN radars, for the intervals during which a circular OCB fit could be made to the IMAGE FUV S113 boundaries, in coordinates relative to the OCB. The contours are determined from data binned in an adjusted latitude bin relative to the OCB location and by 1 h of MLT. (right) The number of vorticity measurements in each bin used in the determination of the average vorticity. The solid lines represent the OCB location.

As in Figure 3, the orange shading relates to a negative vorticity (anticlockwise rotation looking down on the Northern Hemisphere ionosphere) and the blue shading relates to a positive vorticity (clockwise rotation). In this figure the solid red line represents the OCB location, which is fixed. The figure also shows how many measurements have been made in each bin (Figure 4, right), showing that the highest density of measurements are close to, and immediately equatorward of, the OCB location.

The overall morphology of the spatial variation of vorticity across the polar region is similar to that in Figure 3, again clearly matching the R1 and R2 FAC systems. But here it is clear that the OCB is colocated with the peak of the vorticity region associated with R1 FACs. However, there are some clear differences compared to the spatial variation of vorticity presented in Figure 3:

1. In Figure 4 the vorticity regions associated with the R1 FACs are typically more narrow, with sharper boundaries than in Figure 3 (this is particularly clear in the afternoon sector). The largest gradients in vorticity are consequently much closer to the peak. However, contrary to expectations, this region appears broader between dawn and noon than in Figure 3. The reasons for this are unclear at this time.
2. In Figure 4 the vorticity regions associated with the R2 FACs are clearer and more homogeneous than in Figure 3. The R2 vorticity values are also much smaller than those seen at the lowest latitudes in Figure 3.

4.3. Subdivision by IMF Direction

So far we have presented a single average vorticity pattern with no consideration of how this pattern may change with external factors. As discussed in section 1, ionospheric convection varies significantly with the direction of the IMF, and the development of useful climatologies and models requires consideration of factors such as this. Although we are using a relatively small data set, which limits the subdivision of data, it is still important, as part of this demonstration, to investigate variations with IMF direction.

In Figure 5 we present the spatial variation of average vorticity in the OCB-normalized frame for four different IMF directions (as described in the methodology above). The IMF bins are 90° wide and centered on the directions shown on the clock dial in the center of the figure which represents the GSM Y-Z plane. The amount of data points are approximately 13%, 27%, 12%, and 23% of those in Figure 4 for the B_z -positive, B_y -positive, B_z -negative, and B_y -negative directions, respectively. The reduction in the amount of data in each bin will obviously introduce more noise into the climatological patterns, but there are enough data to show the key features with some clarity.

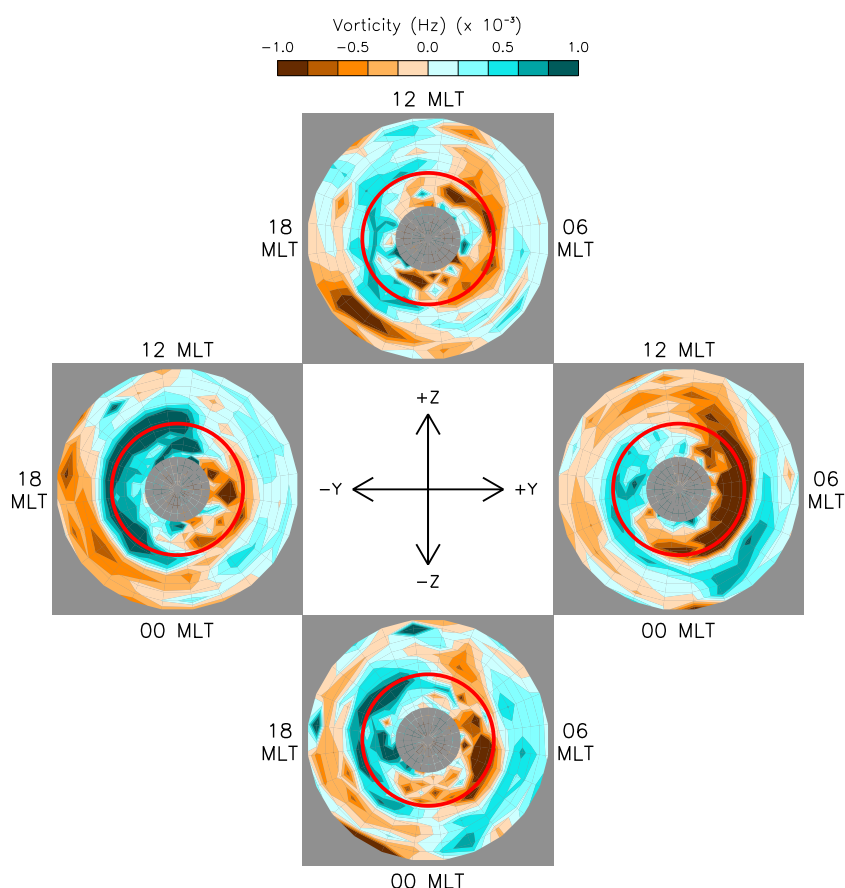


Figure 5. Average vorticity patterns separated by IMF clock angle direction, in coordinates relative to the OCB (see text for full detail). The central direction of each 90° clock angle bin for each map is shown by the dial in the center. Vorticity data were only used from intervals during which a circular OCB fit could be made to the IMAGE FUV SI13 boundaries. Vorticity measurements were only used from half-hour intervals during which at least 70% of the IMF clock angle measurements in that half hour were within a single clock angle bin. The contours are determined from data binned in an adjusted latitude bin relative to the OCB location and by 1 h of MLT. The solid lines represent the OCB location.

We can make the following points about this figure:

1. Although they show the same clear R1 and R2 spatial variation, the IMF B_z -positive and B_z -negative patterns are noisy, and hence difficult to interpret beyond the basic R1/R2 structure.
2. The IMF B_y -dominated patterns show clear spiral structures (as was seen in *Chisham et al.* [2009]) with a very strong R1 vorticity at dawn for IMF B_y -positive, and a very strong R1 vorticity at dusk for IMF B_y -negative. Once again these R1 vorticity regions are centered on the OCB (shown by the red line in Figure 5), and are more narrow and sharp than those presented in *Chisham et al.* [2009].

Although Figure 5 shows the consequences of binning the data with respect to the OCB location, it is clear that more data are needed to clarify the variations that exist with changes in the IMF clock angle direction.

5. Discussion

5.1. Regarding the Impact of Binning Measurements Relative to the OCB Location

As ionospheric convection models and climatologies become a more integral and important part of operational space weather nowcasting and forecasting applications, it is important for these models to be as accurate as possible. The aim of this study was to provide a demonstration of the effect of binning measurements relative to the OCB when developing new ionospheric empirical models and climatologies. One goal was to test whether this new methodology reduces the smoothing of climatological patterns that results from latitudinal variations in the OCB location (due to expansion and contraction of the polar cap) when binning in a fixed geomagnetic coordinate system. Although the climatologies developed in this demonstration were

on a relatively low-resolution spatial grid (due to fairly limited data), they have clearly shown that sharp and narrow features in climatological vorticity maps that occur near the OCB location are heavily smoothed when the data are not binned relative to the OCB location. This smoothing could have severe implications for certain space weather applications where accurate ionospheric convection electric field models play an important role. For example,

1. The tracking of ionospheric plasma density enhancements such as polar patches, that can disrupt and attenuate radio communications through the ionosphere: Ionospheric convection electric field models are crucial for accurately tracking the progress of enhanced regions of electron density [e.g., Zhang *et al.*, 2013]. Accurate ionospheric convection models are needed to help mitigate their effect on HF communication and navigation systems.
2. Estimating the effect of Joule heating on the atmospheric drag on satellites: The combination of ionospheric electric field models with ionospheric conductance measurements or models allows the estimation of Joule heating rates in the ionosphere [e.g., Knipp *et al.*, 2005]. Enhanced Joule heating can increase the atmospheric drag on low Earth orbit spacecraft and hence vary their orbits and significantly decrease their lifetime. As the Joule heating is proportional to the square of the electric field, sharp gradients in the ionospheric electric potential pattern, which are significantly reduced by smoothing, result in much greater Joule heating.
3. Mapping ionospheric electric field models to the magnetosphere to facilitate the estimation of $E \times B$ drift in radiation belt modeling: Energetic particles in the Earth's radiation belts can cause significant damage to components on multimillion pound satellites [e.g., Horne *et al.*, 2013]. In the absence of in situ measurements, large-scale radiation belt models require models of the magnetospheric electric field. This electric field plays an important role in the motion of low-energy particles whose motion is dominated by $E \times B$ drift. These low-energy particles often provide the seed populations for more energetic radiation belt particle populations. In addition, low-energy electrons can damage satellites through surface charging.

5.2. Regarding Potential Issues With the Methodology

The new methodology introduced in this paper has been presented in a way that shows its benefits in the simplest way possible. However, it is important to be aware of any issues that may either prove an impediment to the practical implementation of the methodology, or which might affect the accuracy of the resultant models and climatologies. In the first instance we have identified the following potential issues:

5.2.1. The Limited Availability of OCB Measurements

Measurements of the OCB location are crucial to both the development of models using this methodology, and the use of these models in a practical way (such as in applications), i.e., the size and location of the climatological patterns need to be adjusted for the particular circumstances in which they are being applied. As shown earlier in this paper, smaller OCB data sets will not always provide the extensive, routine measurements needed to develop high-resolution climatologies for a wide range of background conditions.

We have used PALB measurements from spacecraft auroral images to provide good polar-wide OCB estimates. However, at the present time there is no active spacecraft mission that includes an auroral imager capable of imaging the complete auroral oval across the whole polar region. Hence, use of this exact methodology is presently limited to the epochs that were covered by spacecraft missions such as IMAGE (with the FUV instrument) and POLAR (with the UVI instrument). Future missions that provide continual large-scale auroral imaging capability have been proposed, such as the Chinese and European mission Kua-Fu [Milan *et al.*, 2012]. The chance to implement this methodology on a regular basis highlights the importance of such missions.

Given the limited availability of auroral image data, it may be necessary to investigate other proxies for the OCB that provide good coverage over the polar region at a relatively high cadence, such as the convection reversal boundary (CRB) [Sotirelis *et al.*, 2005]. The CRB is relatively easily determined from ionospheric velocity measurements such as those made by the SuperDARN HF radars. However, CRB measurements also have their shortcomings; they are rarely continuous and generally do not cover the whole polar region. There are also some uncertainties regarding the consistency of the relationship between the CRB and the OCB (i.e., the latitudinal offsets between them may vary somewhat). However, further work exploring the relationship between the CRB and the OCB may lead to a greater availability and coverage of other suitable OCB proxies.

5.2.2. Do the Measurements Need to Be Ordered By a Low-Latitude Convection Boundary As Well As the OCB?

In this demonstration, we have chosen to use a binning grid which contains the same number of bins equatorward of the OCB location as there are poleward, which are of the same latitudinal size, and which extend for the same latitudinal extent. Hence, the resulting climatologies focus on variations in relationship to the OCB. However, ionospheric convection generally extends only a limited distance equatorward of the OCB location to the point at which the ionospheric electric field is dominated by corotation. In applications such as the SuperDARN “map potential” analysis, the resultant electric potential solution is scaled by the location of the Heppner-Maynard boundary (HMB) [Heppner and Maynard, 1987; Shepherd and Ruohoniemi, 2000], which is assumed to be colocated with the lower latitude limit of ionospheric convection. Although the variations in the location of the HMB do not change the binning of data in the map potential analysis, the model solution is restricted to within this region.

It is not clear at the present time what effect (if any) the omission of a low-latitude convection boundary has on the development of climatologies. However, what is clear is that introducing this additional boundary into our proposed methodology adds an extra layer of complexity and introduces a new range of issues:

1. We have shown that the amount of usable data is reduced when only intervals where the OCB can be measured are included. Having to continually determine two different boundaries would likely further reduce the data set.
2. The low-latitude convection boundary determined from SuperDARN data is estimated as the lowest possible HMB location outside of which there is no backscatter. This estimation of the low-latitude convection boundary can be unreliable. There are many factors that control the spatial occurrence of SuperDARN backscatter that could result in errors in the HMB placement.
3. If this extra boundary was implemented as part of the present methodology, it would require the low-latitude convection boundary and OCB to be represented by concentric circles. The HMB is not circular and has a fixed center, which is unlikely to be colocated with the center of the OCB circle.

Investigating these issues further would require a major development in the proposed methodology.

5.3. Regarding Other Influences on High-latitude Ionospheric Climatologies and Models

In section 1 of this paper we discussed how it is necessary to produce models and climatologies for a range of IMF and dipole tilt conditions in order to accurately portray the range of spatial variations that are seen across the ionosphere in patterns of ionospheric convection and other electrodynamic processes. However, variations that exist due to other potential influencing factors will be averaged together in the model patterns. Hence, it is important to consider the other factors that influence ionospheric electrodynamics, the influences of which are being removed. These influences could be considered in future models and climatologies and might increase the scope of their practical applicability.

5.3.1. The Influence of Nightside Processes

Nightside reconnection processes, and particularly substorms, are a major driver of ionospheric electrodynamics and significantly change the spatial morphology of convection and FACs in the nightside ionosphere [e.g., Grocott *et al.*, 2002, 2009]. Increased nightside reconnection is also responsible for increasing the cross-polar cap potential drop. The effect of nightside processes on convection is rarely considered in empirical models beyond the indirect effect of the varying IMF, and hence significant variability is averaged away in these model patterns. Weimer [2001b] concluded that the IMF alone was insufficient to predict the electric potential patterns when substorms were present; convection is heavily increased during substorms due to nightside reconnection. Although Weimer [2001b] introduced a reliance on the AL index as an optional controlling parameter they concluded that it does not wholly reproduce the substorm influence in a satisfactory way.

5.3.2. The Influence of Geomagnetic Activity

The influence of geomagnetic activity has significant overlap with other factors as the activity level is closely related to the level of reconnection activity on both the dayside and nightside of the magnetosphere. Geomagnetic activity is clearly associated with the size of polar cap and the magnitude of the cross-polar cap potential. However, there is a question as to whether it results in major changes in the morphology of convection. The development of some ionospheric convection climatologies have investigated variations with K_p [Holt *et al.*, 1987; Peymirat and Fontaine, 1997; Zhang *et al.*, 2007] showing a clear dependence and suggesting that changes in morphology do occur.

5.3.3. The Influence of IMF Clock Angle Timescales

Recently, *Grocott and Milan* [2014] studied how the morphology of ionospheric convection varies with the length of time that a similar IMF clock angle has been maintained prior to the interval of study. They showed that for timescales of up to ~30 min, the convection patterns closely resemble their time-averaged counterparts. However, for greater timescales they concluded that the convection evolves away from these time-averaged patterns producing markedly different convection structures.

6. Conclusions

In this paper we present a demonstration of the application of a new methodology for the development of ionospheric climatologies and empirical models, such as those of the ionospheric convection electric field. The new methodology involves binning measurements used for the model development in a coordinate frame that is ordered by the location of the OCB. It is shown that ignoring the location of the OCB when binning data results in a smoothing of sharp variations in parameters that are seen close to the OCB location, leading to an inadequacy in the climatological models. We use the example of climatological patterns of ionospheric vorticity to demonstrate this. In this demonstration there are sharp maxima in the ionospheric vorticity pattern at the OCB location, associated with the Region 1 FAC system, when the measurements are binned in the OCB-normalized coordinate frame. When the measurements are binned in a fixed geomagnetic coordinate frame, these maxima are heavily smoothed. The results of this analysis have implications for other statistical models determined in this way, such as those for FACs and ionospheric convection velocity and electric field. We have discussed how accuracy in the development of climatologies and models of these parameters is highly important for the next generation of space weather applications.

Acknowledgments

This study is part of the British Antarctic Survey Polar Science for Planet Earth Programme. It was funded by the Natural Environment Research Council. The authors would like to thank the NASA Space Physics Data Facility and National Space Science Data Center. The IMAGE FUV data are provided courtesy of the instrument PI Stephen Mende (University of California, Berkeley). We thank the PI, the IMAGE mission, and the IMAGE FUV team for data usage and processing tools. The raw IMAGE data, and software, are available from <http://sprg.ssl.berkeley.edu/image/>. The auroral boundary data set, and the full methodology used to create it, are available from the author. The author acknowledges the use of SuperDARN data. SuperDARN is a collection of radars funded by the national scientific funding agencies of Australia, Canada, China, France, Japan, South Africa, United Kingdom, and United States of America. The SuperDARN vorticity database, and the software used to produce it, are available from the author.

References

- Anderson, B. J., H. Korth, C. L. Waters, D. L. Green, and P. Stauning (2008), Statistical Birkeland current distributions from magnetic field observations by the Iridium constellation, *Ann. Geophys.*, **26**, 671–687.
- Boakes, P. D., S. E. Milan, G. A. Abel, M. P. Freeman, G. Chisham, B. Hubert, and T. Sotirelis (2008), On the use of IMAGE FUV for estimating the latitude of the open/closed magnetic field line boundary in the ionosphere, *Ann. Geophys.*, **26**, 2759–2769.
- Carbary, J., T. Sotirelis, P. Newell, and C.-I. Meng (2003), Auroral boundary correlations between UVI and DMSP, *J. Geophys. Res.*, **108**(A1), 1018, doi:10.1029/2002JA009378.
- Chisham, G., et al. (2007), A decade of the Super Dual Auroral Radar Network (SuperDARN): Scientific achievements, new techniques and future directions, *Surv. Geophys.*, **28**, 33–109.
- Chisham, G., et al. (2008a), Remote sensing of the spatial and temporal structure of magnetopause and magnetotail reconnection from the ionosphere, *Rev. Geophys.*, **46**, RG1004, doi:10.1029/2007RG000223.
- Chisham, G., T. K. Yeoman, and G. J. Sofko (2008b), Mapping ionospheric backscatter measured by the SuperDARN HF radars—Part 1: A new empirical virtual height model, *Ann. Geophys.*, **26**, 823–841.
- Chisham, G., M. P. Freeman, G. A. Abel, W. A. Bristow, A. Marchaudon, J. M. Ruohoniemi, and G. J. Sofko (2009), Spatial distribution of average vorticity in the high-latitude ionosphere and its variation with interplanetary magnetic field direction and season, *J. Geophys. Res.*, **114**, A09301, doi:10.1029/2009JA014263.
- Cousins, E. D. P., and S. G. Shepherd (2010), A dynamical model of high-latitude convection derived from SuperDARN plasma drift measurements, *J. Geophys. Res.*, **115**, A12329, doi:10.1029/2010JA016017.
- Cowley, S. W. H. (1981), Magnetospheric asymmetries associated with the Y component of the IMF, *Planet. Space Sci.*, **28**, 79–96.
- Cowley, S. W. H., and M. Lockwood (1992), Excitation and decay of solar wind-driven flows in the magnetosphere-ionosphere system, *Ann. Geophys.*, **10**, 103–115.
- Dungey, J. W. (1961), Interplanetary field and auroral zones, *Phys. Rev. Lett.*, **6**, 47–48.
- Foster, J. C., T. Fuller-Rowell, and D. S. Evans (1989), Quantitative patterns of large-scale field-aligned currents in the auroral ionosphere, *J. Geophys. Res.*, **94**, 2555–2564.
- Greenwald, R. A., et al. (1995), DARN/SuperDARN: A global view of the dynamics of high-latitude convection, *Space Sci. Rev.*, **71**, 761–796.
- Grocott, A., and S. E. Milan (2014), The influence of IMF clock angle timescales on the morphology of ionospheric convection, *J. Geophys. Res. Space Physics*, **119**, 5861–5876, doi:10.1002/2014JA020136.
- Grocott, A., S. W. H. Cowley, J. B. Sigwarth, J. F. Watermann, and T. K. Yeoman (2002), Excitation of twin-vortex flow in the nightside high-latitude ionosphere during an isolated substorm, *Ann. Geophys.*, **20**, 1577–1601.
- Grocott, A., J. A. Wild, S. E. Milan, and T. K. Yeoman (2009), Superposed epoch analysis of the ionospheric convection evolution during substorms: Onset latitude dependence, *Ann. Geophys.*, **27**, 591–600.
- Haaland, S. E., G. Paschmann, M. Förster, J. M. Quinn, R. B. Torbert, C. E. McIlwain, H. Vaith, P. A. Puhl-Quinn, and C. A. Kletzing (2007), High-latitude plasma convection from Cluster EDI measurements: Method and IMF-dependence, *Ann. Geophys.*, **25**, 239–253.
- Heppner, J. P. (1972), Polar cap electric field distributions related to the interplanetary magnetic field direction, *J. Geophys. Res.*, **77**, 4877–4887.
- Heppner, J. P. (1977), Empirical models of high-latitude electric fields, *J. Geophys. Res.*, **82**, 1115–1125.
- Heppner, J. P., and N. C. Maynard (1987), Empirical high-latitude electric field models, *J. Geophys. Res.*, **92**, 4467–4489.
- Holt, J. M., R. H. Wand, J. V. Evans, and W. L. Oliver (1987), Empirical models for the plasma convection at high latitudes from Millstone Hill observations, *J. Geophys. Res.*, **92**, 203–232.
- Holzworth, R. H., and C.-I. Meng (1975), Mathematical representation of the auroral oval, *Geophys. Res. Lett.*, **2**, 377–380.
- Horne, R. B., S. A. Glauert, N. P. Meredith, D. Boscher, V. Maget, D. Heynderickx, and D. Pitchford (2013), Space Weather impacts on satellites and forecasting the Earth's electron radiation belts with SPACECAST, *Space Weather*, **11**, 169–186, doi:10.1002/swe.20023.

- Knipp, D. J., T. Welliver, M. G. McHarg, F. K. Chun, W. K. Tobiska, and D. Evans (2005), Climatology of extreme upper atmospheric heating events, *Adv. Space Res.*, **36**, 2506–2510.
- Longden, N., G. Chisham, M. P. Freeman, G. A. Abel, and T. Sotirelis (2010), Estimating the location of the open-closed magnetic field line boundary from auroral images, *Ann. Geophys.*, **28**, 1659–1678.
- McWilliams, K. A., T. K. Yeoman, J. B. Sigwarth, L. A. Frank, and M. Brittner (2001), The dayside ultraviolet aurora and convection responses to a southward turning of the interplanetary magnetic field, *Ann. Geophys.*, **19**, 707–721.
- Mende, S. B., et al. (2000a), Far ultraviolet imaging from the IMAGE spacecraft. 1. System design, *Space Sci. Rev.*, **91**, 243–270.
- Mende, S. B., et al. (2000b), Far ultraviolet imaging from the IMAGE spacecraft. 2. Wideband FUV imaging, *Space Sci. Rev.*, **91**, 271–285.
- Mende, S. B., et al. (2000c), Far ultraviolet imaging from the IMAGE spacecraft. 3. Spectral imaging of the Lyman- α and OI 135.6 nm, *Space Sci. Rev.*, **91**, 287–318.
- Meng, C.-I., R. H. Holzworth, and S.-I. Akasofu (1977), Auroral circle—Delineating the poleward boundary of the quiet auroral belt, *J. Geophys. Res.*, **82**, 164–172.
- Milan, S. E., et al. (2012), KuaFu: Exploring the Sun-Earth connection, *Astron. Geophys.*, **53**, 4.21–4.24.
- Newell, P., W. Burke, E. Sánchez, C.-I. Meng, M. Greenspan, and C. Clauer (1991), The low-latitude boundary layer and the boundary plasma sheet at low altitude: Prenoon precipitation regions and convection reversal boundaries, *J. Geophys. Res.*, **96**, 21,013–21,023.
- Newell, P., Y. Feldstein, Y. Galperin, and C.-I. Meng (1996), Morphology of nightside precipitation, *J. Geophys. Res.*, **101**, 10,737–10,748.
- Papitashvili, V. O., and F. J. Rich (2002), High-latitude ionospheric convection models derived from Defense Meteorological Satellite Program ion drift observations and parameterized by the interplanetary magnetic field strength and direction, *J. Geophys. Res.*, **107**(A8), 1198, doi:10.1029/2001JA000264.
- Pettigrew, E. D., S. G. Shepherd, and J. M. Ruohoniemi (2010), Climatological patterns of high-latitude convection in the Northern and Southern Hemispheres: Dipole tilt dependencies and interhemispheric comparisons, *J. Geophys. Res.*, **115**, A07305, doi:10.1029/2009JA014956.
- Peymirat, C., and D. Fontaine (1997), Polar cap convection patterns inferred from EISCAT observations, *Ann. Geophys.*, **15**, 403–411.
- Rich, F. J., and M. Hairston (1994), Large-scale convection patterns observed by DMSP, *J. Geophys. Res.*, **99**, 3827–3844.
- Rich, F. J., and N. C. Maynard (1989), Consequences of using simple analytical functions for the high-latitude convection electric field, *J. Geophys. Res.*, **94**, 3687–3701.
- Richmond, A. D. (1992), Assimilative mapping of ionospheric electrodynamics, *Adv. Space Res.*, **12**(6), 59–68.
- Ridley, A. J. (2007), Effects of seasonal changes in the ionospheric conductances on magnetospheric field-aligned currents, *Geophys. Res. Lett.*, **34**, L05101, doi:10.1029/2006GL028444.
- Ruohoniemi, J. M., and K. B. Baker (1998), Large-scale imaging of high-latitude convection with Super Dual Auroral Radar Network HF radar observations, *J. Geophys. Res.*, **103**, 20,797–20,811.
- Ruohoniemi, J. M., and R. A. Greenwald (1996), Statistical patterns of high-latitude convection obtained from Goose Bay HF radar observations, *J. Geophys. Res.*, **101**, 21,743–21,763.
- Ruohoniemi, J. M., and R. A. Greenwald (2005), Dependencies of high-latitude plasma convection: Consideration of interplanetary magnetic field, seasonal, and universal time factors in statistical patterns, *J. Geophys. Res.*, **110**, A09204, doi:10.1029/2004JA010815.
- Russell, C. T. (1972), The configuration of the magnetosphere, in *Critical Problems of Magnetospheric Physics*, edited by E. R. Dyer, pp. 1–16, Natl. Acad. of Sci., Washington, D. C.
- Russell, C. T., Y. L. Wang, and J. Raeder (2003), Possible dipole tilt dependence of dayside magnetopause reconnection, *Geophys. Res. Lett.*, **30**(18), 1937, doi:10.1029/2003GL017725.
- Shepherd, S. G., and J. M. Ruohoniemi (2000), Electrostatic potential patterns in the high-latitude ionosphere constrained by SuperDARN measurements, *J. Geophys. Res.*, **105**, 23,005–23,014.
- Siscoe, G. L., and T. S. Huang (1985), Polar cap inflation and deflation, *J. Geophys. Res.*, **90**, 543–547.
- Sofko, G. J., R. A. Greenwald, and W. Bristow (1995), Direct determination of large-scale magnetospheric field-aligned currents with SuperDARN, *Geophys. Res. Lett.*, **22**, 2041–2044.
- Sotirelis, T., and P. T. Newell (2000), Boundary-oriented electron precipitation model, *J. Geophys. Res.*, **105**, 18,655–18,673.
- Sotirelis, T., P. T. Newell, and C.-I. Meng (1998), Shape of the open-closed boundary of the polar cap as determined from observations of precipitating particles by up to four DMSP satellites, *J. Geophys. Res.*, **103**, 399–406.
- Sotirelis, T., J. M. Ruohoniemi, R. J. Barnes, P. T. Newell, R. A. Greenwald, J. P. Skura, and C.-I. Meng (2005), Comparison of SuperDARN radar boundaries with DMSP particle precipitation boundaries, *J. Geophys. Res.*, **110**, A06302, doi:10.1029/2004JA010732.
- Umbach, D., and K. N. Jones (2003), A few methods for fitting circles to data, *IEEE Trans. Instrum. Meas.*, **52**, 1881–1885.
- Villain, J.-P., C. Hanuise, and G. Caudal (1985), A SAFARI-EISCAT comparison between the velocity of F region small-scale irregularities and the ion drift, *J. Geophys. Res.*, **90**, 8433–8443.
- Weimer, D. R. (1995), Models of high-latitude electric potentials derived with a least error fit of spherical harmonic coefficients, *J. Geophys. Res.*, **100**, 19,595–19,607.
- Weimer, D. R. (2001a), An improved model of ionospheric electric potentials including substorm perturbations and application to the Geospace Environment Modeling November 24, 1996, event, *J. Geophys. Res.*, **106**, 407–416.
- Weimer, D. R. (2001b), Maps of ionospheric field-aligned currents as a function of the interplanetary magnetic field derived from Dynamics Explorer 2 data, *J. Geophys. Res.*, **106**, 12,889–12,902.
- Weimer, D. R. (2005), Improved ionospheric electrodynamic models and application to calculating Joule heating rates, *J. Geophys. Res.*, **110**, A05306, doi:10.1029/2004JA010884.
- Weimer, D. R., D. M. Ober, N. C. Maynard, W. J. Burke, M. R. Collier, D. J. McComas, N. F. Ness, and C. W. Smith (2002), Variable time delays in the propagation of the interplanetary magnetic field, *J. Geophys. Res.*, **107**(A8), 1210, doi:10.1029/2001JA009102.
- Yeoman, T. K., G. Chisham, L. J. Baddeley, R. S. Dhillon, T. J. T. Karhunen, T. R. Robinson, A. Senior, and D. M. Wright (2008), Mapping ionospheric backscatter measured by the SuperDARN HF radars—Part 2: Assessing SuperDARN virtual height models, *Ann. Geophys.*, **26**, 843–852.
- Zhang, S.-R., J. M. Holt, and M. McCready (2007), High latitude convection based on long-term incoherent scatter radar observations in North America, *J. Atmos. Sol. Terr. Phys.*, **69**, 1273–1291.
- Zhang, Q.-H., et al. (2013), Direct observations of the evolution of polar cap ionization patches, *Science*, **339**, 1597–1600.